An Origin of North American Monsoon Retreat Biases in Climate Models

JIACHENG YE[a] AND ZHUO WANG[a]

[a] *University of Illinois at Urbana–Champaign, Urbana, Illinois*

(Manuscript received 5 August 2022, in final form 1 February 2023, accepted 15 March 2023)

ABSTRACT: Many coupled climate models suffer from a late retreat bias in North American monsoon (NAM) simulations, which is manifested by overestimated precipitation in October. The overestimated precipitation has long been attributed to the negative sea surface temperature (SST) biases in the tropical Atlantic and insufficient model resolution to resolve mesoscale features. However, we found little correlation between CMIP6 model resolutions and the simulated NAM retreat-season precipitation in October. Instead, we showed that tropical eastern North Pacific SST biases and the associated large-scale circulation biases play a dominant role in inducing the retreat-season biases, with SST biases in other ocean basins playing a secondary role. As revealed by simulations using a hierarchy of models, the positive SST biases in the tropical eastern North Pacific enhance local convection and lead to positive diabatic heating biases throughout the troposphere; the diabatic heating biases generate a Matsuno–Gill type of response that strengthens the subtropical high over the North Atlantic and weakens the subtropical high over the North Pacific, enhancing the low-level northward moisture transport from the tropics to the NAM region. The conclusion is robust across phase 6 of CMIP (CMIP6) models. The precipitation seasonality in the NAM region is used to constrain future projection. The "good" CMIP6 models project that the timing of the NAM peak season remains the same, but the peak-season precipitation is reduced and monsoon retreat is delayed, while the "poor" CMIP6 models project a delayed monsoon peak season with slightly enhanced peak-season precipitation. Both model groups project a drier dry season in the NAM region.

KEYWORDS: Monsoons; Climate models; Climate change; Precipitation; Diabatic heating; Bias

1. Introduction

The North American monsoon (NAM) is one of the most prominent hydrological features over southwest North America in summer. It is characterized by an abrupt increase of precipitation in May and June, a peak monsoon season from July to early September that accounts for over 60% of local annual precipitation, and a quick retreat in October accompanied by substantial changes in large-scale circulation (Higgins et al. 1997). Different from its East Asian counterpart, the NAM is unique in that it resides between the Gulf of California (GoC) to the west and the Gulf of Mexico (GoM) to the east and is shaped by the narrow Sierra Madre Occidental (SMO) mountains spanning from the Arizona–Mexico border to southwestern Mexico, stretching about 1100 km. GoC and GoM are regarded as two main moisture sources for NAM precipitation, although their relative contributions are debatable (e.g., Schmitz and Mullen 1996; Dominguez et al. 2016; Jana et al. 2018). Low-level moisture surges, characterized by an anomalous southeasterly flow over the GoC, often precede NAM precipitation on the synoptic scale (Hales 1972; Brenner 1974; Pascale and Bordoni 2016). The GoC surges are often associated with tropical easterly waves or tropical cyclones on the synoptic time scale (e.g., Favors and Abatzoglou 2013; Seastrand et al. 2015; Pascale and Bordoni 2016). Additionally, the GoC surges can be modulated by large-scale tropical and extratropical atmospheric variability on the subseasonal scale, including the quasi-biweekly (QBW) mode and the Madden–Julian oscillation (Lorenz and Hartmann 2006; Douglas and Leal 2003; Fuller and Stensrud 2000; Johnson et al. 2007; Kikuchi and Wang 2009). A realistic representation of the NAM in global climate circulation models thus may require improvements across different time scales. Additionally, fine topological features also affect NAM simulations. Boos and Pascale (2021) suggested that the NAM should be regarded as convectively enhanced orographic rainfall over the SMO instead of a thermally forced tropical monsoon.

Most climate models, however, have difficulty simulating the seasonal cycle of NAM precipitation. Liang et al. (2008) examined the performance of the phase 3 of the Coupled Model Intercomparison Project (CMIP3) models in representing NAM precipitation, and they found that CMIP3 models showed little consistency in the precipitation annual cycle and commonly overestimated the retreat-season precipitation.

Supplemental information related to this paper is available at the Journals Online website: https://doi.org/10.1175/JCLI-D-22-0592.s1.

Ye's current affiliation: University of Chicago, Chicago, Illinois.

Corresponding author: Zhuo Wang, zwang.jas@ametsoc.org

DOI: 10.1175/JCLI-D-22-0592.1

Geil et al. (2013) and Cook and Seager (2013) showed that CMIP5 models showed little improvements compared to CMIP3 models, and that precipitation biases remained common among both model groups (e.g., Torres-Alavez et al. 2014; Pascale et al. 2017; Wang et al. 2020). However, only a limited number of studies have investigated the cause of the retreat-season biases. Liang et al. (2008) hypothesized that SST biases in the subtropical eastern Pacific and the GoM were major contributors, but the hypothesis was not tested in climate models. Geil et al. (2013) suggested that the retreat of the subtropical highs in climate models directed low-level wind and moisture transport from the eastern North Pacific to the west coast of Mexico, leading to precipitation biases in the core monsoon region. The origin of the biases of the subtropical high evolution, however, remains unraveled. Based on a set of coupled GCM experiments with and without flux adjustment, Pascale et al. (2017) suggested that systematic SST biases contributed to the retreat-season precipitation biases, but further examination of the source regions of SST biases and the associated mechanisms remained to be done.

Owing to higher model resolution and more advanced subgrid parameterizations, CMIP6 models show a general improvement in representing the internal modes of climate variability and the spatiotemporal distribution of precipitation, moisture, and wind, compared to CMIP5 and CMIP3 models (Bock et al. 2020; Lee et al. 2021) and also have an overall more realistic representation of the East Asian monsoon and Indian monsoon system (Xin et al. 2020; Gusain et al. 2020). However, studies regarding the performance of the NAM simulation in CMIP6 models are relatively limited. According to a recent NAM overview study across phases 5 and 6 of the CMIP (Hernandez and Chen 2022), CMIP6 models show a good agreement with observations on the overall timing of the monsoon onset and decay and a slight reduction in wet biases throughout the year, but the positive precipitation biases remain during the monsoon retreat season.

In this study, we investigate the origin of retreat-season precipitation biases and attempt to constrain NAM future projection using the precipitation seasonality. For convenience, October will be referred to as the NAM retreat season, following some previous studies (e.g., Lin et al. 2008; Cook and Seager 2013; Geil et al. 2013). October represents the most characteristic features of the season mean during October–November. Focusing on October also helps relax the model selection given that some climate models provide limited access to daily data. The remainder of the study is organized as follows: Section 2 includes the description of the models, data, and methodology. The performance of CMIP6 models in the NAM simulation and the associated large-scale circulation biases and their causes are examined in section 3. Section 4 assesses the future projection of the NAM. Discussion and summary are presented in the last section.

2. Data, model, and methodology

a. Climate model output and evaluation datasets

Twenty-six CMIP6 models and 25 Atmospheric Model Intercomparison Project (AMIP) models (Eyring et al. 2016) are analyzed in this study (Table S1 in the online supplemental material). NorESM2-MM is included in the CMIP model selection but not in the AMIP model selection because it was unavailable at the time of analysis. In AMIP simulations, SSTs and sea ice concentrations (SICs) are prescribed based on observations (Eyring et al. 2016). The configurations of the CMIP models, except for an interactive oceanic component, and the applied historical forcings (e.g., solar variability, volcanic aerosols, anthropogenic emissions) are identical to those of the corresponding AMIP models. The comparison between AMIP and CMIP simulations thus allows us to quantify the impacts arising from the oceanic processes. The historical simulations during 1979–2014 are examined for the present climate, and the period of 2065–2100 is used to assess the future climate. We examine the Shared Socioeconomic Pathways (SSP) 585 for the future projection. SSP 585 represents the worst warming scenario, with the radiative forcing stabilized at 8.5 W m^{-2} in 2100 and offers an opportunity to extract a robust signal of how the NAM system will evolve in the future. Due to the large data volume, only one ensemble member from each model is included, and our evaluation is focused on multimodel means (MMMs). For brevity, fully coupled and AMIP-type simulations are denoted as CMIP and AMIP, respectively.

Datasets used to evaluate model simulations include monthly mean SST from the Hadley Centre Sea Ice and Sea Surface Temperature (HadISST), version 1.1 (Rayner et al. 2003), monthly mean precipitation from Global Precipitation Climatology Project (GPCP), version 2.3 (Adler et al. 2003), and variables [i.e., geopotential height, horizontal wind, specific humidity, air temperature, pressure velocity, and precipitation (only for GoC surge diagnostics)] from the ERA5 reanalysis (Hersbach et al. 2020). All observational, reanalysis, and modeling variables are regridded to the horizonal resolution of 1° × 1° before analysis.

b. Community Earth System Model

To investigate how SST biases in different regions may contribute to circulation biases, numerical simulations based on CESM, version 2.1.3 (Danabasoglu et al. 2020) are carried out with prescribed SSTs. The simulations were carried out using the scientifically validated component set F2000climo, which employs CAM6 physics and is run at the horizontal resolution of 0.9° × 1.25°. The prescribed monthly mean SST and sea ice in the control run are obtained from a merged product (Hurrell et al. 2008) based on the HadISST1 and Optimum Interpolation Sea Surface Temperature dataset, version 2 (OISST2; Reynolds et al. 2002), during the period of 1995–2005, which is identical to the SST fields used to drive the AMIP simulations. The control and sensitivity experiments including GLOBAL, NEPAC20N, HEMEHIS20N, and NEHEMIS30N are all initialized on 1 January 2000 and are first run for six months to the end of June. Ten ensemble members for each experiment are then initialized again on 1 July by adding small random perturbations to the temperature and specific humidity fields, and each member is further integrated for five more months to the end of November to allow the consideration of internal variability. Information about the sensitivity and control simulations is listed in Table 1. In the GLOBAL experiment, the

TABLE 1. Description of each CESM2.1.3 experiment.

Experiment	SST forcing
CONTROL	Observed monthly mean SST during 1995–2005
GLOBAL	Monthly mean CMIP6 MMM SST during 1995–2005 over the global oceans
NEPAC20N	Same as the Control expt, except that SST over 0°–20°N, 180°–270°E is replaced by the CMIP6 MMM SST
NEHEMIS20N	Same as the Control expt, except that SST over 0°–20°N, 180°–360° is replaced by the CMIP6 MMM SST
NEHEMIS30N	Same as the Control expt, except that SST over 0°–30°N, 180°–360° is replaced by the CMIP6 MMM SST

global SST field is replaced by the SST field derived from the CMIP6 MMM. The SST differences between the MMM and observation in October are shown in Fig. S4a. For the other sensitivity experiments, the SST field is replaced by the CMIP6 MMM SST in different regions to investigate the relative importance of regional SST biases on the NAM simulations. The replacement areas are further outlined in Fig. S4b.

c. *Simple stationary wave model*

In addition to CESM simulations, we carried out a set of simulations using a simple linear stationary wave model (SWM) developed by Ting and Yu (1998) to investigate the response of the NAM circulation to regional diabatic heating biases. The model is built upon linearized vorticity equations adapted from the NOAA/GFDL spectral model with R30 resolution (approximately 3.75° longitude × 2.25° latitude) and 24 vertical layers, and it is driven by diabatic heating, transient eddy forcing, and orographic forcing. Boos and Pascale (2021) applied a variant of this model with finer horizontal resolution (R63) and highlighted the dominant role of orographic effects in producing local monsoonal precipitation, which demonstrated the usefulness of the SWM in studying the NAM mechanisms.

Most CMIP6 models only provide daily historical output at limited vertical levels (i.e., eight vertical levels from 1000 to 10 hPa). Our analysis reveals that the NAM retreat biases in the CESM2.1 are similar to the other CMIP6 models. We thus derive the SWM forcing terms from the CESM2.1 daily output, which is available at 32 vertical levels (https://www.earthsystemgrid.org/dataset/ucar.cgd.cesm2.output.html). To be consistent with the forcing terms, the basic state of the SWM is derived from the long-term (1979–2014) mean atmospheric state from the CESM2.1 fully coupled experiments in October.

Information about the sensitivity and control simulations is listed in Table 2. In the control experiment (SWM_Control), the basic state, transient forcing, and diabatic forcing are all derived from the CESM2.1 CMIP-type simulation. As shown later in section 3 (see Fig. 1a), the retreat-season precipitation bias in AMIP models is much weaker than that in CMIP models. We will thus focus on the differences between AMIP and CMIP models. Tests with each forcing term (not shown here) showed that the impacts of transient momentum fluxes on the subtropical and tropical circulation are at least an order of magnitude smaller than that of diabatic heating. We will thus focus on testing the effects of diabatic heating in the SWM experiments. In the sensitivity experiments, the three-dimensional diabatic heating field in different regions is replaced by that derived from the CESM2.1 AMIP-type simulations, while the other forcing terms and the basic state remain unchanged. All simulations are integrated for 100 days, and the averages over days 30–100 are taken for the diagnostics.

d. *Identification of GoC surges*

GoC surges are characterized by an intermittent, lower-level, southwesterly flow over the gulf area. We adopt a GoC surge index proposed by Pascale and Bordoni (2016), which is based on two leading principal components (PC1 and PC2) of an empirical orthogonal function (EOF) analysis of the summertime [June–September (JJAS)] daily meridional 10-m wind averaged from ERA5 6-hourly output. The first two EOFs account for 81% (58% for EOF1 and 23% for EOF2) of the spatiotemporal variability. EOF1 is characterized by a southerly flow extending from south to north along the GoC, corresponding to the most impactful surges. The EOF2 is characterized by a southerly flow north of 25°N and a northerly flow south of 25°N, corresponding to a weak surge scenario. GoC surges from July to September (JAS) account for 61% of rainfall in the NAM core region, slightly lower than their contributions over Arizona and western New Mexico (~70%; Pascale et al. 2016), possibly due to the more limited local moisture source over the inland monsoon area.

To identify GoC surges in October, we project the daily 10-m meridional wind anomaly in October onto the EOF1 and

TABLE 2. SWM experiments and the diabatic heating replacement domains (depicted by green lines in Fig. S2). The names for the replacement experiments ("SWM_AABB_CCDDX") start with "SWM" and indicate the zonal bound ("AABB") and meridional bound ("CCDDX").

Experiment name	Diabatic heating replacement domain	Experiment name	Diabatic heating replacement domain
SWM_CTRL	—	SWM_AMIP	Global
SWM_0090_0020N	0°–20°N, 0°–90°E	SWM_180270_0020N	0°–20°N, 180°–270°E
SWM_0090_0020S	0°–20°S, 0°–90°E	SWM_180270_0020S	0°–20°S, 180°–270°E
SWM_90180_0020N	0°–20°N, 90°E–180°	SWM_270360_0020N	0°–20°N, 270°E–360°
SWM_90180_0020S	0°–20°S, 90°E–180°	SWM_270360_0020S	0°–20°S, 270°E–360°
SWM_outside_20S20Nocean	20°S–20°N, 0°–360°	SWM_outside_20S20Nconti	20°S–20°N, 0°–360°

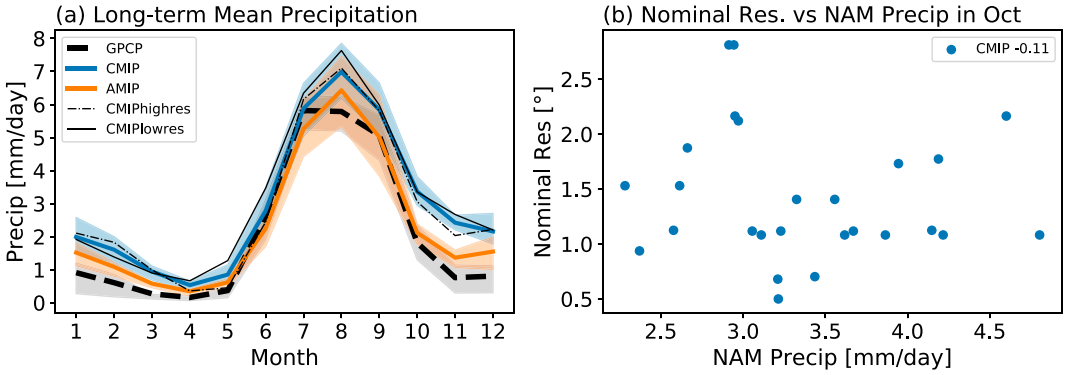

FIG. 1. (a) Climatological monthly mean precipitation (mm day^{-1}) in the NAM core region (shown in Fig. S1) from GPCP (black), CMIP MMM (blue), and AMIP MMM (orange), with shading of the corresponding color representing the range of 25th and 75th percentiles. Thin solid and dashed lines represent the means from the four models of the highest and lowest resolutions, respectively. (b) The scatterplot of NAM precipitation and climate model nominal resolution.

EOF2 derived from ERA5 daily data during JAS, and the PC1 and PC2 (normalized by the standard deviation in JAS during 1979–2014 from the ERA5 or the corresponding model simulations) are used to identify a surge event as follows. Potential surge days are defined as the days when either PC1 or PC2 is above 0.75. Consecutive surge days are then grouped into surge events. Each surge event has to be separated by at least one nonsurge day when the PC1 and PC2 are both less than 0.75. Since the NAM precipitation sometimes has a delayed response to a GoC surge (Pascale and Bordoni 2016), surge events are extended by one day when calculating surge-associated precipitation. GoC surges contribute to 67% of the total rainfall in October according to the assessment using the ERA5 daily precipitation data during 1979–2014, highlighting the important role of GoC surges in modulating the NAM precipitation even in the retreat season. We also examined EOFs of meridional wind from each GCM. The EOF modes are similar to those derived from the ERA5. However, we prefer the surge identification method based on EOFs derived from the ERA5 because it is model independent and can accurately depict the essential characteristics of surge events.

3. Link between large-scale circulation and NAM retreat-season precipitation bias

a. *Simulated NAM precipitation and its relation to large-scale circulation biases*

The monsoon core area (denoted by red grid points to the west of the SMO in Fig. S1) is defined based on the fraction of summertime rainfall to the total annual amount no less than 60%. Figure 1a shows the climatological monthly mean precipitation from the CMIP and AMIP simulations in monsoonal core region, along with the GPCP precipitation. Compared to the CMIP, the AMIP precipitation exhibits a more realistic annual cycle, including substantially reduced precipitation bias in October. Some previous studies suggest that models with higher resolution have a better representation of mesoscale processes, complex terrain, and GoC surges and thus have a better representation of the NAM (Castro et al. 2012; Bukovsky et al. 2013; Meyer and Jin 2016, 2017; Varuolo-Clarke et al. 2019). The four CMIP6 models with the highest horizontal resolution have slightly smaller biases in the precipitation annual cycle, including slightly reduced precipitation biases in October, compared to the four models with lowest resolution. However, the biases in these higher-resolution models are still much larger than those in the AMIP simulations. Additionally, the correlation between the retreat-season precipitation and model nominal resolution is merely −0.11 (Fig. 1b), which is statistically insignificant. Although it is possible that those higher resolutions are still too coarse to resolve small-scale processes and thus to substantially improve the NAM representation (Geil et al. 2013), it is likely that the precipitation biases are mainly induced by other factors. In particular, the much smaller precipitation biases in the AMIP simulations imply the crucial role of a realistic SST field in reducing NAM precipitation biases. One of the most significant differences between the CMIP and AMIP observation occurs in the retreat season, when the CMIP MMM overestimates the precipitation by more than 1 mm day^{-1}, persisting to the postmonsoon season. As discussed in the previous section, the retreat season biases are not well studied. We will thus investigate the differences between CMIP and AMIP simulations in October in the following analysis, with a special focus on the impacts of SST biases.

Figure 2a shows the difference in geopotential height and horizontal wind at 850 hPa between CMIP and AMIP MMM in October (similar patterns are also found in November but are not as distinctive as in October). Compared to the AMIP, the CMIP produces a stronger North Atlantic subtropical high (NASH) and a weaker North Pacific subtropical high (NPSH). Together, they act to strengthen lower-level northeastward wind from the tropical eastern North Pacific to the NAM region in the CMIP, which enhances the moisture transport to the NAM region and leads to strong moisture flux convergence along the coast (Fig. 2b).

To assess the effect of subtropical high biases, we defined a subtropical-high index based on 850-hPa geopotential height difference between the NPSH and NASH regions ($GP_{atl} - GP_{pac}$; purple boxes in Fig. 2a). The scatterplot between the subtropical

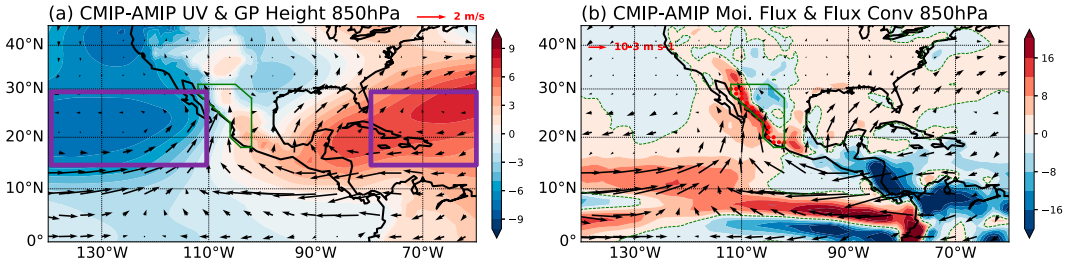

FIG. 2. Differences of 850-hPa (a) geopotential height (shading; gpm) and horizontal wind, and (b) horizontal moisture flux and moisture flux convergence (shading; 10^{-9} kg kg^{-1} s^{-1}) between CMIP and AMIP MMM. The purple boxes in (a) denote the North Pacific (140°–110°W, 15°–30°N) and North Atlantic (80°–60°W, 15°–30°N) subtropical high regions used to calculate the subtropical high index, and the NAM core area is highlighted by red dots in (b). To aid visualization of the NAM region, the area delimited by green lines represents the generalized monsoon area.

high index and retreat-season precipitation (Fig. 3) reveals a strong linear relationship ($r \sim 0.7$). Although correlation does not necessarily mean causality, it implies the strong control of the large-scale circulation on NAM precipitation that is supported by the analysis in the subsequent sections. While this dynamic control helps explain the difference between the AMIP and CMIP, it is interesting to note that such a link also exists in the AMIP simulations despite there being a weaker correlation ($r \sim 0.53$). That the AMIP simulations are all forced by the same observed SST field indicates that model structural differences, in addition to SST differences, can also contribute to the biases of the two subtropical highs. A significant correlation between the subtropical high index and precipitation is also found in SSP585 simulations. The correlation coefficient is slightly weaker, possibly due to the displacements of the subtropical highs in the future climate simulations (Li et al. 2012).

b. *Attribution of retreat-season biases based on stationary wave model simulations*

We use SWM simulations to investigate the role of diabatic heating biases in generating circulation biases in this section. Figure 4a shows the differences in 850-hPa streamfunction

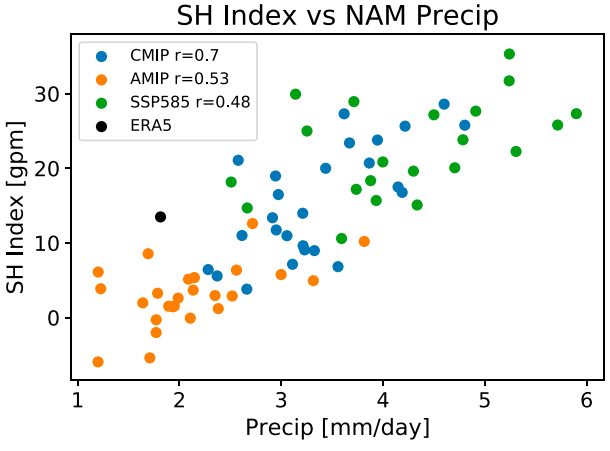

FIG. 3. Scatterplot between the subtropical high index (SH = $GP_{atl} - GP_{pac}$; gpm) and NAM precipitation (mm day^{-1}) in October. The linear correlations are indicated in the color key.

and horizontal wind in October between the CESM CMIP and CESM AMIP experiments. The difference pattern suggests a strengthened and westward extended NASH and a weakened NPSH in the CMIP simulations. The anomalous northward low-level flow is consistent with the differences between the CMIP and AMIP MMM in Fig. 2a except with a slight zonal displacement and is largely captured by the SWM when the global diabatic heating field derived from the CESM CMIP-type simulations is replaced by that derived from the CESM AMIP-type simulations (i.e., SWM_CTRL minus SWM_AMIP; Figs. 4b,c). To explore how diabatic heating in different regions contributes to the modification of the two subtropical highs, a suite of regional diabatic heating replacement experiments are performed (Table 2). In these experiments, we replace the diabatic heating derived from the CESM CMIP-type simulations with that derived from the CESM AMIP-type simulations in different regions over the tropical (20°S–20°N) and extratropical (poleward of 20° latitude) oceans. The rest of the forcing terms and the basic state are kept. Additional replacement experiments are also performed over the continental area.

In the first set of experiments, we equally divide tropical oceans (20°S–20°N) into eight regions (excluding land; Figs. S2a–h), and in the second set of experiments, we examine the role of the diabatic heating over the extratropical oceans and continents (Fig. S2i and Fig. 2j). Comparison of 10 experiments shows that the diabatic heating anomalies over the tropical northeastern North Pacific play the most important role in producing NAM-related, large-scale circulation biases (Fig. 4d or Fig. S2e). The 850-hPa wind and geopotential height differences over the North Pacific and North America (Fig. 4d) have a spatial pattern similar to the response differences when the global diabatic heating is replaced, although the former are weaker (Fig. 4c). Larger differences exist over the Indian Ocean–west Pacific (as seen between Figs. 4c and 4d), which can be attributed to the local heating differences in that sector (including both oceanic and continental regions; Fig. S2). The upper-level circulation response (250 hPa; Fig. S3) over the tropical and subtropical eastern North Pacific is nearly opposite to the lower-level response and consistent with the typical Matsuno–Gill pattern. The opposite biases of the NASH and NPSH in the CMIP simulations are thus primarily forced by the same mechanism and can be linked to the

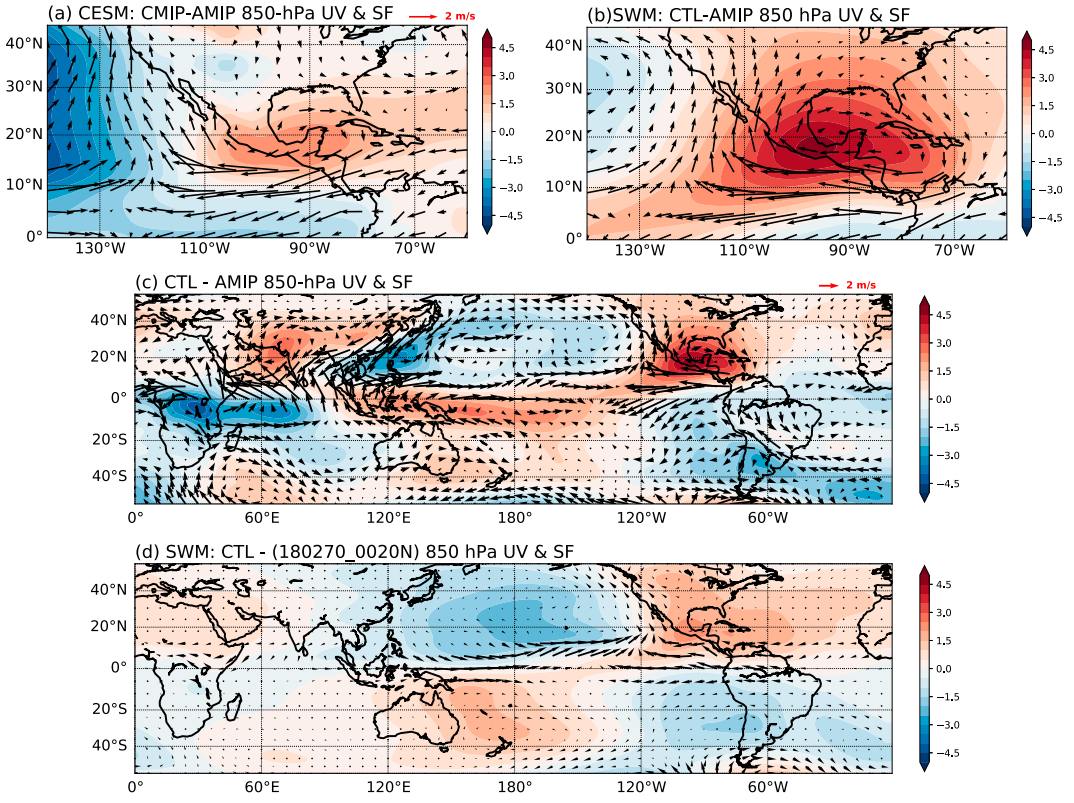

FIG. 4. (a) Differences of 850-hPa streamfunction (SF; shading; 10^6 kg s^{-1}) and horizontal wind (arrows) in October between the CESM CMIP- and AMIP-type simulations. (b) The differences between SWM_CTRL and SWM_AMIP. (c) As in (b), but from a global view; (d) as in (c) but for the differences between SWM_CTRL and SWM_180270_0020N.

diabatic heating biases over the eastern North Pacific. The anomalous northward lower-level flow is a direct consequence of such an effect.

Figure 5a shows the vertical profile of diabatic heating over the tropical eastern North Pacific, which clearly shows that the diabatic heating derived from the CESM CMIP simulations is overestimated throughout the free troposphere. In contrast, the diabatic heating derived from the CESM AMIP simulations is closer to that of the ERA5 reanalysis, which provides one of the best heating estimates among reanalyses (e.g., Hoffmann et al. 2019; X. Chen et al. 2020). Although the SWM simulations are based on heating fields derived from the CESM simulations, the mechanism is likely important in all CMIP6 models. We found a strong correlation between the vertical integral of the diabatic heating and the subtropical high index in October ($r = 0.79$; not shown) and a strong correlation ($r = 0.76$) between the diabatic heating and NAM precipitation (Fig. 5b) for CMIP models, suggesting that overestimated diabatic heating leads to enhanced lower-level northward flow from the tropical eastern Pacific to the NAM region and induces excessive precipitation.

Another interesting finding is that the diabatic heating biases over the global land generate a circulation anomaly to the west of the NAM core (Fig. S2j). Although the anomalous cyclonic circulation (surrounding the GoC) is much weaker and does not collocate with the weakened NPSH over the eastern Pacific, this anomalous cyclonic circulation helps strengthen and redirect the lower-level northward flow to the east, as in the CMIP simulations.

c. *Exploring the origin of diabatic heating biases using CESM experiments*

To explore the origin of diabatic heating biases over the tropical eastern North Pacific, we performed a suite of AGCMs using CESM2.1.3. The control experiment is driven by the observed SST field while SST biases (with respect to observations) from the CMIP MMM (Fig. S4a) are added to different regions in the sensitivity experiments (i.e., the observed SST is replaced by the SST field derived from the CMIP MMM in different regions; see Table 1). The SST biases in the CMIP models are characterized by prevailing cold biases in extratropical oceans. Large warm biases exist over subtropical eastern oceans extending westward. Such SST biases have been a long-standing issue in CMIP models and reduce only moderately from CMIP5 to CMIP6 (Richter and Tokinaga 2020), which can probably be attributed to the deficiencies of GCMs in representing low cloud–SST feedback in subtropical eastern oceans (Myers et al. 2021). The tropical eastern Pacific (~0°–20°N, ~150°–90°W) is also subject to warm SST biases. Additionally, prevailing cold SST biases are found over the North Atlantic, which could be attributed to the weaker-than-normal Atlantic meridional

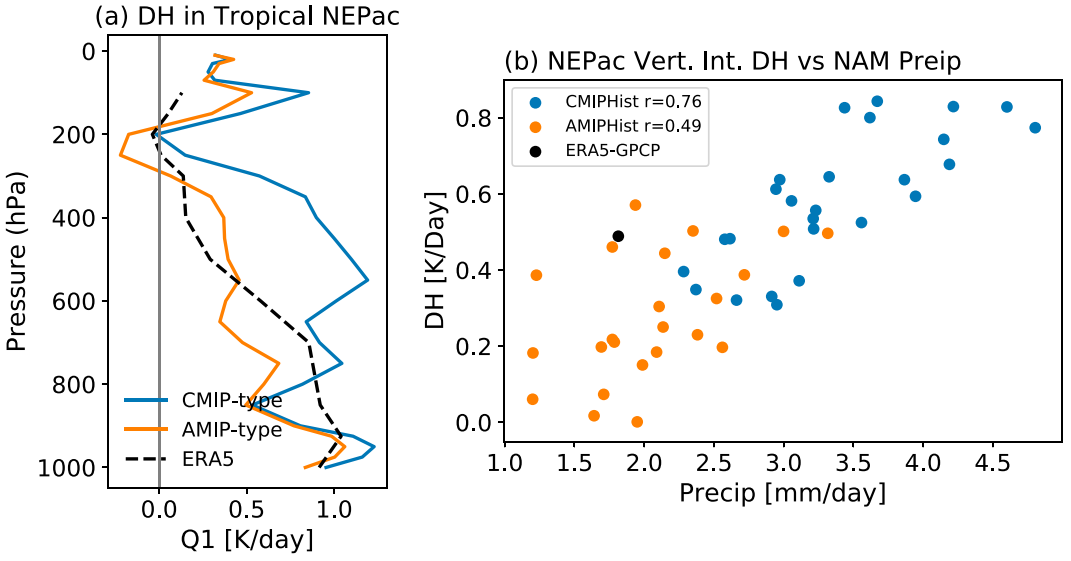

FIG. 5. (a) Vertical profile of diabatic heating (DH) in the tropical eastern North Pacific (0°–20°N, 150°–90°W) for the CESM CMIP-type (blue) and AMIP-type (orange) simulations and the ERA5 reanalysis (black) in October (1979–2014). (b) Scatterplot between diabatic heating and NAM precipitation in October from the CMIP (blue) and AMIP (orange) models. The black dot denotes the long-term mean diabatic heating derived from the ERA5 and GPCP precipitation. The diabatic heating is calculated using monthly data.

overturning circulation (AMOC) in CMIP models (Wang et al. 2014) and linked to SST biases in the North Pacific (Johnson et al. 2020).

Figure 6 shows the biases of 850-hPa geopotential height and horizontal wind relative to the control experiment for each sensitivity experiment. When the observed SST is replaced by CMIP MMM SST globally (Fig. 6a), the response of 850-hPa geopotential height is similar to the CMIP–AMIP differences (Fig. 2a), characterized by the westward extension and strengthening of NASH and weakening of NPSH. This suggests that SST biases, instead of the representation of air–sea coupling, make the major contribution to the differences between AMIP and CMIP MMM. When the CESM is driven by CMIP MMM SST in the tropical eastern North Pacific SST only (Fig. 6b), the responses of two subtropical highs are largely reproduced (Fig. 6a). When the replaced SST is extended to the tropical North Atlantic (NEHemis20N experiment; 0°–20°N, 180°–360°), the NASH is substantially intensified (Fig. 6c). This suggests that the basin-wide negative SST biases over the tropical Atlantic help strengthen the local

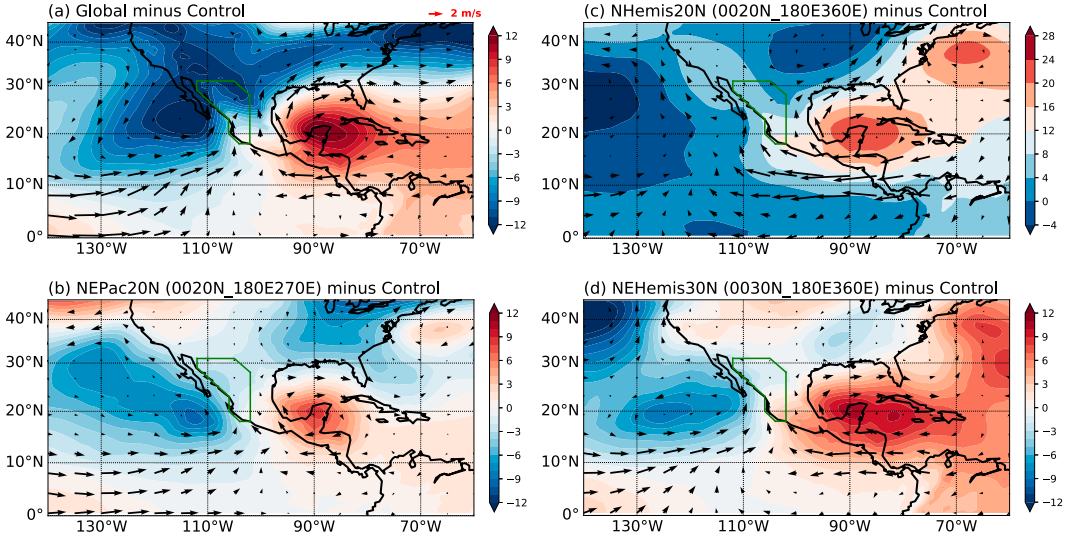

FIG. 6. (a)–(d) Differences of 850-hPa geopotential height (shading; gpm) and horizontal wind between different SST replacement experiments and the CESM control experiment. Note that the color bar in (c) is different from those in the other three panels.

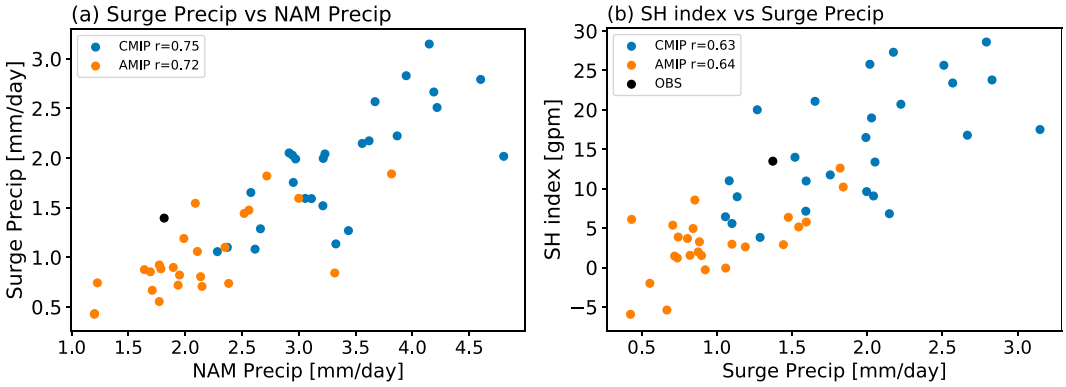

FIG. 7. Scatterplot between (a) the surge-related precipitation (mm day^{-1}) and NAM precipitation in October and (b) the subtropical high index (gpm) and surge-related precipitation in October. Linear correlations are also indicated in the figure legends.

subtropical high. The intensified NASH might be regarded as a direct response to the cold SST biases, consistent with the finding of Johnson et al. (2020) about the impacts of SST biases on cold-season precipitation over North America. Furthermore, when the subtropical SST off the west of the California coast is also replaced in the NEHemis30N experiment (Fig. 6d), the NASH is further enhanced while the negative biases associated with the NPSH shift toward the west coast of North America. The NPSH-related, negative geopotential height biases off the coast may be related to the local positive SST biases via the SST–low cloud–circulation feedback. The dynamical and physical mechanisms linking trade wind zone SST biases and lower-level circulation biases are not fully understood. However, it is possible that the deficiencies in the representation of surface wind stress, the atmospheric heat flux, and the intrinsic error in the atmospheric general circulation model are the major culprits (Koseki et al. 2018). Weakened NPSH and strengthened NASH are also found in an SWM experiment in which the diabatic heating is replaced over the extratropical oceans (Outside_20S20Nocean; Fig. S2i).

We also examined the vertical profile of diabatic heating averaged over the tropical eastern North Pacific in different experiments (Fig. S5). The diabatic heating in the control experiment is close to the AMIP MMM. The NEPac20N experiment, which replaces the tropical eastern North Pacific SST, shows stronger diabatic heating than that of the control experiment and lies in the middle between the control experiment and the GLOBAL experiment, indicating the important role of the local SST biases. As SST biases from more ocean areas are included in an experiment (from NEPac20N to NEHemis30N), the diabatic heating becomes increasingly overestimated, suggesting that SST biases affect the subtropical highs in a constructive way.

Given the strong link between GoC surges and NAM precipitation, it is possible that SST biases also contribute to biases related to GoC surges. A strong correlation between October NAM core precipitation and GoC surge-related precipitation is found in both CMIP models ($r = 0.75$) and AMIP models ($r = 0.72$) (Fig. 7a), indicating that higher retreat-season precipitation is associated with higher surge-related precipitation. Further analysis (Fig. 7b) reveals a strong positive correlation (~0.6) between the subtropical high index and surge-related precipitation (Fig. 7b), suggesting that higher surge-related rainfall can be partly attributed to the subtropical high intensity. This is likely due to a stronger mean northward flow associated with a stronger subtropical high index that can enhance the total moisture transport during a surge event.

4. Future changes of the NAM system

Large uncertainties exist in the future projection of the NAM precipitation due to deficiencies of model physics, SST biases, etc. (e.g., Geil et al. 2013; Z. Chen et al. 2020). In this section we attempt to constrain the projection uncertainty based on the model representation of precipitation seasonality. We use relative entropy to assess precipitation seasonality (Feng et al. 2013; Pascale et al. 2015). We then select a set of "good" models and a set of "poor" models and examine their future projections of the NAM in SSP585. Projections based on SSP 585 help to reveal the changes of the NAM evolution in the worst warming scenario.

The relative entropy (Kullback and Leibler 1951) can quantitatively measure the similarity between two probability distributions without any prior assumptions about the distribution formula. It is defined as

$$R = \sum_i p_i \log\left(\frac{p_i}{q_i}\right), \tag{1}$$

where p_i is the reference (i.e., ERA5) distribution, and q_i is referred to as the simulated distribution. R is a nonnegative value, with the zero value corresponding to a perfect simulated distribution identical to the reference distribution. We examine the long-term monthly mean precipitation including nonmonsoon season normalized by the annual total precipitation in the monsoon core region. The observed long-term mean (1979–2014) from the GPCP is used as the reference distribution, and the simulated distribution is derived from the same historical period. The assumption is that the models capturing the observed precipitation seasonality could more reliably project the future changes of the monsoon retreat.

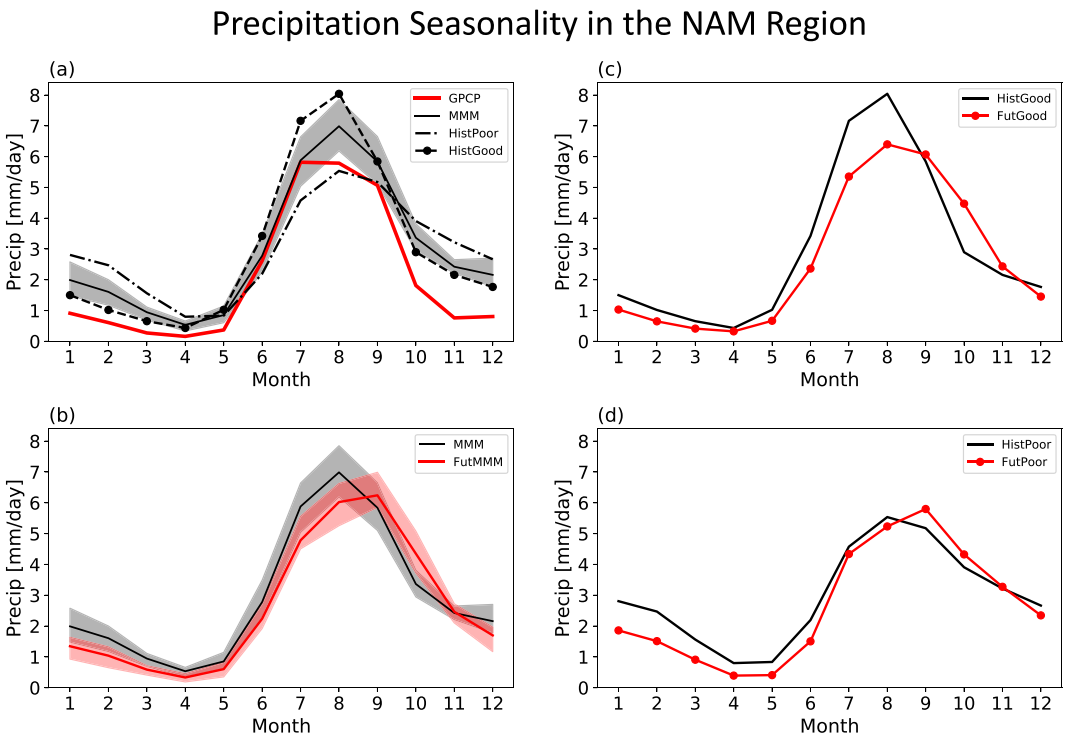

FIG. 8. Long-term mean monthly precipitation for (a) historical (1979–2014) GPCP long-term mean, CMIP MMM, and CMIP poor- and good-model mean; (b) historical CMIP MMM and future (1965–2100) SSP585 MMM; (c) CMIP good-model means for the historical period and the future projection; and (d) CMIP poor-model means for the historical period and the future projection. Shading represents the range of 25th and 75th percentiles in (a) and (b).

Based on the relative entropy, four models (i.e., HadGEM3-GC31-LL, NorESM2-MM, BCC-ESM1, and CanESM5) are chosen as good models and four models (i.e., CNRM-CM6–1-HR, MRI-ESM2, CESM2-FV2, and FGOALS-f3-L) are chosen as poor models. The historical simulations of good models exhibit a better seasonality with higher-than-MMM precipitation during the monsoon onset (June) and mature season (July–August) and lower-than-MMM precipitation during the retreat (October–November) and dry season (December–March) (Fig. 8). In contrast, the poor models have a weaker seasonality, a drier monsoon season, and a wetter dry season. For the future climate (2065–2100), the MMM projects a delayed monsoon season cycle that peaks in September, in contrast to the August peak in the historical MMM simulations; the peak monsoon precipitation is slightly reduced, and the dry season is projected to become drier, while the precipitation in October is projected to increase. Regarding the good models, the monsoon onset and peak time in the future projection are the same as in the historical runs. Similar to the MMM, there is an overall reduction in precipitation in all months except from September to November, which indicates a delayed monsoon retreat. Different from the good models, the poor models project a stronger monsoon peak in September, while the retreat-season precipitation increases only moderately. In addition, the poor models project a drier dry season, consistent with both the MMM and good model projections.

The drier monsoon season projected by good models is largely consistent with the findings of Pascale et al. (2017) based on the flux-adjusted climate model projections. They suggested that the precipitation decline during the peak monsoon season can be attributed to increased atmospheric stability and the resultant weakened convection. The underlying mechanisms for the different future projections in good and poor models are beyond the scope of this study and are left for future investigation.

5. Summary and discussion

The simulations of the NAM in CMIP models suffer from a common retreat-season bias characterized by overestimated rainfall in October. We investigated the origin of this bias in this study using a hierarchy of models. Our analysis shows that higher model resolution cannot effectively reduce the retreat-season precipitation biases among CMIP6 models. In contrast, the retreat-season bias is substantially reduced in the AMIP model simulations that are driven by observed SSTs. Compared to the AMIP MMM, the CMIP MMM produces a stronger NASH and a weaker NPSH, leading to an anomalous lower-level flow from the tropics to the NAM core region and an overestimated moisture transport. A subtropical high index, representing the differences between the two subtropical highs, is highly correlated to the retreat-season NAM precipitation among models, demonstrating a close relationship between the

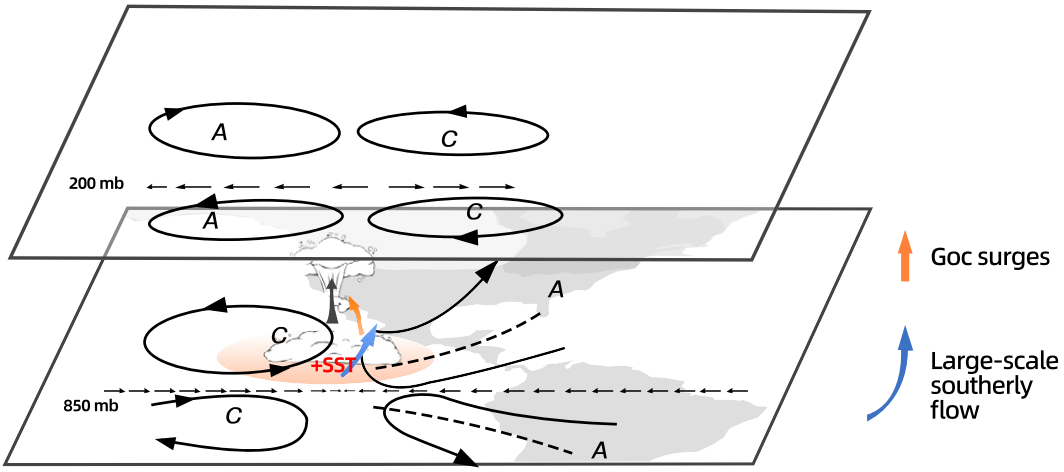

FIG. 9. Diagram of how regional SST biases are related to the NAM retreat bias.

large-scale circulation biases and NAM retreat-season precipitation bias is robust across different models.

The SWM experiments suggest that the positive diabatic heating biases over the tropical eastern North Pacific play a dominant role in strengthening the NPSH and weakening the NASH via a Matsuno–Gill pattern response. The biases in NPSH and NASH together act to generate an anomalous northward flow from the tropics. In addition, the diabatic heating biases over other oceanic basins as well as extratropical land also modify the spatial pattern and magnitude of the lower-level moisture transport from the GoC to the monsoon inland area.

To examine which regional SST biases contribute to the diabatic heating biases over the eastern North Pacific, we conducted a suite of SST replacement experiments using the CESM. We show that the positive SST biases in the tropical eastern North Pacific are a dominant factor. SST biases in other regions (including the subtropical eastern Pacific and the tropical North Atlantic Ocean) play a secondary role in generating the subtropical high biases. Further analysis shows that GoC surge-related precipitation is closely related to the subtropical high index and NAM precipitation, suggesting that GoC surges connect large-scale circulation biases to the mesoscale NAM retreat-season biases, consistent with the multiscale nature of the NAM (e.g., Berbery 2001; Mejia et al. 2016). A conceptual diagram of how the NAM system is linked back to SST biases over the tropical eastern North Pacific by the Matsuno–Gill mechanism is suggested in Fig. 9.

Future change of the NAM system is also examined based on the evaluation of the precipitation seasonality using relative entropy. Compared with the historical period (1979–2014), the CMIP MMM from SSP 585 projects a delayed monsoon peak in September (in contrast to the August peak in the present climate simulations), and precipitation is reduced in the dry season and the monsoon mature season but increased in October, indicating a delayed monsoon retreat. The good models project the same monsoon peak month in August as in the present climate but project a larger reduction in peak monsoon precipitation than the CMIP MMM and a more pronounced delayed retreat. In contrast, the poor models predicted a delayed monsoon peak in September with enhanced precipitation. It is worth noting that all model groups project a drier dry season in the NAM region.

Our study overall highlights the role of large-scale circulation biases in producing NAM precipitation biases, in contrast to mesoscale representation of GoCs or topography. The large-scale circulation biases can be traced back to SST biases via diabatic heating biases. However, retreat-season precipitation biases also exist in AMIP models, despite a smaller magnitude. This implies that other factors, such as model physics and insufficient model resolution, contribute partly to the NAM retreat-season biases. In addition, this study is implicitly built upon the assumption that the tropical atmosphere is driven by SST anomalies via diabatic heating. Such a simplified view helps trace model biases, but active air–sea coupling exists in the tropics, and land–atmosphere interaction is an important factor modulating the monsoon circulation and precipitation. It is possible that some model errors originate from the atmosphere but are amplified by air–sea interaction or land–ocean–atmosphere interaction, which contribute to the large biases in CMIP models. For example, the low-level wind associated with the NPSH is an active player in air–sea interaction over the subtropical eastern North Pacific. The biases in the NPSH may be thus linked to and amplified by the biases in SST and boundary layer low clouds in this region. We hope our study helps shed light on these long-standing complex problems, which certainly merit further investigation.

Acknowledgments. This work is supported by the National Oceanic and Atmospheric Administration (NOAA) Grant NA18OAR4310271. We acknowledge the NCAR Computational and Information Systems Laboratory (CISL) for providing data access and thank Dr. Mingfang Ting for making the stationary wave model available. We would also like to thank Dr. Chuan-Chieh Chang for stimulating discussions and assistance in numerical model simulations.

Data availability statement. The CMIP6 dataset is available online and can be accessed from https://esgf-node.llnl.gov/projects/cmip6/. The ERA5 are available through the NCAR Research Data Archive (RDA) (https://rda.ucar.edu/datasets/ds630.0), and GPCP, version 2.3, precipitation data can be accessed through https://www.ncei.noaa.gov/access/metadata/landing-page/bin/iso?id=gov.noaa.ncdc:C00979. Sea surface temperature data (HadISST) are available from Hadley Centre (https://www.metoffice.gov.uk/hadobs/hadisst/). Climate Data Gateway at NCAR (https://www.earthsystemgrid.org/dataset/ucar.cgd.cesm2.output.html) provides daily CMIP6–CESM data.

REFERENCES

Adler, R. F., and Coauthors, 2003: The version 2 Global Precipitation Climatology Project (GPCP) monthly precipitation analysis (1979–present). *J. Hydrometeor.*, **4**, 1147–1167, https://doi.org/10.1175/1525-7541(2003)004<1147:TVGPCP>2.0.CO;2.

Berbery, E. H., 2001: Mesoscale moisture analysis of the North American monsoon. *J. Climate*, **14**, 121–137, https://doi.org/10.1175/1520-0442(2001)013<0121:MMAOTN>2.0.CO;2.

Bock, L., and Coauthors, 2020: Quantifying progress across different CMIP phases with the ESMValTool. *J. Geophys. Res. Atmos.*, **125**, e2019JD032321, https://doi.org/10.1029/2019JD032321.

Boos, W. R., and S. Pascale, 2021: Mechanical forcing of the North American monsoon by orography. *Nature*, **599**, 611–615, https://doi.org/10.1038/s41586-021-03978-2.

Brenner, I. S., 1974: A surge of maritime tropical air—Gulf of California to the southwestern United States. *Mon. Wea. Rev.*, **102**, 375–389, https://doi.org/10.1175/1520-0493(1974)102<0375:ASOMTA>2.0.CO;2.

Bukovsky, M. S., D. J. Gochis, and L. O. Mearns, 2013: Towards assessing NARCCAP regional climate model credibility for the North American monsoon: Current climate simulations. *J. Climate*, **26**, 8802–8826, https://doi.org/10.1175/JCLI-D-12-00538.1.

Castro, C. L., H.-I. Chang, F. Dominguez, C. Carrillo, J.-K. Schemm, and H.-M. Henry Juang, 2012: Can a regional climate model improve the ability to forecast the North American monsoon? *J. Climate*, **25**, 8212–8237, https://doi.org/10.1175/JCLI-D-11-00441.1.

Chen, X., O. M. Pauluis, L. R. Leung, and F. Zhang, 2020: Significant contribution of mesoscale overturning to tropical mass and energy transport revealed by the ERA5 reanalysis. *Geophys. Res. Lett.* **47**, e2019GL085333, https://doi.org/10.1029/2019GL085333.

Chen, Z., T. Zhou, L. Zhang, X. Chen, W. Zhang, and J. Jiang, 2020: Global land monsoon precipitation changes in CMIP6 projections. *Geophys. Res. Lett.*, **47**, e2019GL086902, https://doi.org/10.1029/2019GL086902.

Cook, B. I., and R. Seager, 2013: The response of the North American monsoon to increased greenhouse gas forcing. *J. Geophys. Res. Atmos.*, **118**, 1690–1699, https://doi.org/10.1002/jgrd.50111.

Danabasoglu, G., and Coauthors, 2020: The Community Earth System Model version 2 (CESM2). *J. Adv. Model. Earth Syst.*, **12**, e2019MS001916, https://doi.org/10.1029/2019MS001916.

Dominguez, F., G. Miguez-Macho, and H. Hu, 2016: WRF with water vapor tracers: A study of moisture sources for the North American monsoon. *J. Hydrometeor.*, **17**, 1915–1927, https://doi.org/10.1175/JHM-D-15-0221.1.

Douglas, M. W., and J. C. Leal, 2003: Summertime surges over the Gulf of California: Aspects of their climatology, mean structure, and evolution from radiosonde, NCEP reanalysis, and rainfall data. *Wea. Forecasting*, **18**, 55–74, https://doi.org/10.1175/1520-0434(2003)018<0055:SSOTGO>2.0.CO;2.

Eyring, V., S. Bony, G. A. Meehl, C. A. Senior, B. Stevens, R. J. Stouffer, and K. E. Taylor, 2016: Overview of the Coupled Model Intercomparison Project phase 6 (CMIP6) experimental design and organization. *Geosci. Model Dev.*, **9**, 1937–1958, https://doi.org/10.5194/gmd-9-1937-2016.

Favors, J. E., and J. T. Abatzoglou, 2013: Regional surges of monsoonal moisture into the southwestern United States. *Mon. Wea. Rev.*, **141**, 182–191, https://doi.org/10.1175/MWR-D-12-00037.1.

Feng, X., A. Porporato, and I. Rodriguez-Iturbe, 2013: Changes in rainfall seasonality in the tropics. *Nat. Climate Change*, **3**, 811–815, https://doi.org/10.1038/nclimate1907.

Fuller, R. D., and D. J. Stensrud, 2000: The relationship between tropical easterly waves and surges over the Gulf of California during the North American monsoon. *Mon. Wea. Rev.*, **128**, 2983–2989, https://doi.org/10.1175/1520-0493(2000)128<2983:TRBTEW>2.0.CO;2.

Geil, K. L., Y. L. Serra, and X. Zeng, 2013: Assessment of CMIP5 model simulations of the North American monsoon system. *J. Climate*, **26**, 8787–8801, https://doi.org/10.1175/JCLI-D-13-00044.1.

Gusain, A., S. Ghosh, and S. Karmakar, 2020: Added value of CMIP6 over CMIP5 models in simulating Indian summer monsoon rainfall. *Atmos. Res.*, **232**, 104680, https://doi.org/10.1016/j.atmosres.2019.104680.

Hales, J. E., Jr., 1972: Surges of maritime tropical air northward over the Gulf of California. *Mon. Wea. Rev.*, **100**, 298–306, https://doi.org/10.1175/1520-0493(1972)100<0298:SOMTAN>2.3.CO;2.

Hernandez, M., and L. Chen, 2022: Future land precipitation changes over the North American monsoon region using CMIP5 and CMIP6 simulations. *J. Geophys. Res. Atmos.*, **127**, e2021JD035911, https://doi.org/10.1029/2021JD035911.

Hersbach, H., and Coauthors, 2020: The ERA5 global reanalysis. *Quart. J. Roy. Meteor. Soc.*, **146**, 1999–2049, https://doi.org/10.1002/qj.3803.

Higgins, R. W., Y. Yao, and X. L. Wang, 1997: Influence of the North American monsoon system on the U.S. summer precipitation regime. *J. Climate*, **10**, 2600–2622, https://doi.org/10.1175/1520-0442(1997)010<2600:IOTNAM>2.0.CO;2.

Hoffmann, L., and Coauthors, 2019: From ERA-Interim to ERA5: The considerable impact of ECMWF's next-generation reanalysis on Lagrangian transport simulations. *Atmos. Chem. Phys.*, **19**, 3097–3124, https://doi.org/10.5194/acp-19-3097-2019.

Hurrell, J. W., J. J. Hack, D. Shea, J. M. Caron, and J. Rosinski, 2008: A new sea surface temperature and sea ice boundary dataset for the Community Atmosphere Model. *J. Climate*, **21**, 5145–5153, https://doi.org/10.1175/2008JCLI2292.1.

Jana, S., B. Rajagopalan, M. A. Alexander, and A. J. Ray, 2018: Understanding the dominant sources and tracks of moisture for summer rainfall in the southwest United States. *J. Geophys. Res. Atmos.*, **123**, 4850–4870, https://doi.org/10.1029/2017JD027652.

Johnson, N. C., L. Krishnamurthy, A. T. Wittenberg, B. Xiang, G. A. Vecchi, S. B. Kapnick, and S. Pascale, 2020: The impact of sea surface temperature biases on North American precipitation in a high-resolution climate model. *J. Climate*, **33**, 2427–2447, https://doi.org/10.1175/JCLI-D-19-0417.1.

Johnson, R. H., P. E. Ciesielski, B. D. McNoldy, P. J. Rogers, and R. K. Taft, 2007: Multiscale variability of the flow during the North American Monsoon Experiment. *J. Climate*, **20**, 1628–1648, https://doi.org/10.1175/JCLI4087.1.

Kikuchi, K., and B. Wang, 2009: Global perspective of the quasi-biweekly oscillation. *J. Climate*, **22**, 1340–1359, https://doi.org/10.1175/2008JCLI2368.1.

Koseki, S., N. Keenlyside, T. Demissie, T. Toniazzo, F. Counillon, I. Bethke, M. Ilicak, and M.-L. Shen, 2018: Causes of the large warm bias in the Angola–Benguela frontal zone in the Norwegian Earth System Model. *Climate Dyn.*, **50**, 4651–4670, https://doi.org/10.1007/s00382-017-3896-2.

Kullback, S., and R. A. Leibler, 1951: On information and sufficiency. *Ann. Math. Stat.*, **22**, 79–86, https://doi.org/10.1214/aoms/1177729694.

Lee, J., K. R. Sperber, P. J. Gleckler, K. E. Taylor, and C. J. W. Bonfils, 2021: Benchmarking performance changes in the simulation of extratropical modes of variability across CMIP generations. *J. Climate*, **34**, 6945–6969, https://doi.org/10.1175/JCLI-D-20-0832.1.

Li, W., L. Li, M. Ting, and Y. Liu, 2012: Intensification of Northern Hemisphere subtropical highs in a warming climate. *Nat. Geosci.*, **5**, 830–834, https://doi.org/10.1038/ngeo1590.

Liang, X. Z., J. Zhu, K. E. Kunkel, M. Ting, and J. X. L. Wang, 2008: Do CGCMs simulate the North American monsoon precipitation seasonal–interannual variability? *J. Climate*, **21**, 4424–4448, https://doi.org/10.1175/2008JCLI2174.1.

Lin, J., B. E. Mapes, K. M. Weickmann, G. N. Kiladis, S. D. Schubert, M. J. Suarez, J. T. Bacmeister, and M. Lee, 2008: North American monsoon and convectively coupled equatorial waves simulated by IPCC AR4 coupled GCMs. *J. Climate*, **21**, 2919–2937, https://doi.org/10.1175/2007JCLI1815.1.

Lorenz, D. J., and D. L. Hartmann, 2006: The effect of the MJO on the North American monsoon. *J. Climate*, **19**, 333–343, https://doi.org/10.1175/JCLI3684.1.

Mejia, J. F., M. W. Douglas, and P. J. Lamb, 2016: Observational investigation of relationships between moisture surges and mesoscale-to large-scale convection during the North American monsoon. *Int. J. Climatol.*, **36**, 2555–2569, https://doi.org/10.1002/joc.4512.

Meyer, J. D. D., and J. Jin, 2016: Bias correction of the CCSM4 for improved regional climate modeling of the North American monsoon. *Climate Dyn.*, **46**, 2961–2976, https://doi.org/10.1007/s00382-015-2744-5.

——, and ——, 2017: The response of future projections of the North American monsoon when combining dynamical downscaling and bias correction of CCSM4 output. *Climate Dyn.*, **49**, 433–447, https://doi.org/10.1007/s00382-016-3352-8.

Myers, T. A., R. C. Scott, M. D. Zelinka, S. A. Klein, J. R. Norris, and P. M. Caldwell, 2021: Observational constraints on low cloud feedback reduce uncertainty of climate sensitivity. *Nat. Climate Change*, **11**, 501–507, https://doi.org/10.1038/s41558-021-01039-0.

Pascale, S., and S. Bordoni, 2016: Tropical and extratropical controls of Gulf of California surges and summertime precipitation over the southwestern United States. *Mon. Wea. Rev.*, **144**, 2695–2718, https://doi.org/10.1175/MWR-D-15-0429.1.

——, V. Lucarini, X. Feng, A. Porporato, and S. ul Hasson, 2015: Analysis of rainfall seasonality from observations and climate models. *Climate Dyn.*, **44**, 3281–3301, https://doi.org/10.1007/s00382-014-2278-2.

——, S. Bordoni, S. B. Kapnick, G. A. Vecchi, L. Jia, T. L. Delworth, S. Underwood, and W. Anderson, 2016: The impact of horizontal resolution on North American monsoon Gulf of California moisture surges in a suite of coupled global climate models. *J. Climate*, **29**, 7911–7936, https://doi.org/10.1175/JCLI-D-16-0199.1.

——, W. R. Boos, S. Bordoni, T. L. Delworth, S. B. Kapnick, H. Murakami, G. A. Vecchi, and W. Zhang, 2017: Weakening of the North American monsoon with global warming. *Nat. Climate Change*, **7**, 806–812, https://doi.org/10.1038/nclimate3412.

Rayner, N. A., D. E. Parker, E. B. Horton, C. K. Folland, L. V. Alexander, D. P. Rowell, E. C. Kent, and A. Kaplan, 2003: Global analyses of sea surface temperature, sea ice, and night marine air temperature since the late nineteenth century. *J. Geophys. Res.*, **108**, 4407, https://doi.org/10.1029/2002JD002670.

Reynolds, R. W., N. A. Rayner, T. M. Smith, D. C. Stokes, and W. Wang, 2002: An improved in situ and satellite SST analysis for climate. *J. Climate*, **15**, 1609–1625, https://doi.org/10.1175/1520-0442(2002)015<1609:AIISAS>2.0.CO;2.

Richter, I., and H. Tokinaga, 2020: An overview of the performance of CMIP6 models in the tropical Atlantic: Mean state, variability, and remote impacts. *Climate Dyn.*, **55**, 2579–2601, https://doi.org/10.1007/s00382-020-05409-w.

Schmitz, J. T., and S. L. Mullen, 1996: Water vapor transport associated with the summertime North American monsoon as depicted by ECMWF analyses. *J. Climate*, **9**, 1621–1634, https://doi.org/10.1175/1520-0442(1996)009<1621:WVTAWT>2.0.CO;2.

Seastrand, S., Y. Serra, C. Castro, and E. Ritchie, 2015: The dominant synoptic-scale modes of North American monsoon precipitation. *Int. J. Climatol.*, **35**, 2019–2032, https://doi.org/10.1002/joc.4104.

Ting, M., and L. Yu, 1998: Steady response to tropical heating in wavy linear and nonlinear baroclinic models. *J. Atmos. Sci.*, **55**, 3565–3582, https://doi.org/10.1175/1520-0469(1998)055<3565:SRTTHI>2.0.CO;2.

Torres-Alavez, A., T. Cavazos, and C. Turrent, 2014: Land–sea thermal contrast and intensity of the North American monsoon under climate change conditions. *J. Climate*, **27**, 4566–4580, https://doi.org/10.1175/JCLI-D-13-00557.1.

Varuolo-Clarke, A. M., K. A. Reed, and B. Medeiros, 2019: Characterizing the North American monsoon in the Community Atmosphere Model: Sensitivity to resolution and topography. *J. Climate*, **32**, 8355–8372, https://doi.org/10.1175/JCLI-D-18-0567.1.

Wang, B., C. Jin, and J. Liu, 2020: Understanding future change of global monsoons projected by CMIP6 models. *J. Climate*, **33**, 6471–6489, https://doi.org/10.1175/JCLI-D-19-0993.1.

Wang, C., L. Zhang, S.-K. Lee, L. Wu, and C. R. Mechoso, 2014: A global perspective on CMIP5 climate model biases. *Nat. Climate Change*, **4**, 201–205, https://doi.org/10.1038/nclimate2118.

Xin, X., T. Wu, J. Zhang, J. Yao, and Y. Fang, 2020: Comparison of CMIP6 and CMIP5 simulations of precipitation in China and the East Asian summer monsoon. *Int. J. Climatol.*, **40**, 6423–6440, https://doi.org/10.1002/joc.6590.